



**HAL**  
open science

# Accurate Estimations of Sea-Ice Thickness and Elastic Properties From Seismic Noise Recorded With a Minimal Number of Geophones: From Thin Landfast Ice to Thick Pack Ice

Ludovic Moreau, Jérôme Weiss, David Marsan

► **To cite this version:**

Ludovic Moreau, Jérôme Weiss, David Marsan. Accurate Estimations of Sea-Ice Thickness and Elastic Properties From Seismic Noise Recorded With a Minimal Number of Geophones: From Thin Landfast Ice to Thick Pack Ice. *Journal of Geophysical Research. Oceans*, 2020, 125, pp.2141-2167. 10.1029/2020JC016492 . insu-03594474

**HAL Id: insu-03594474**

**<https://insu.hal.science/insu-03594474v1>**

Submitted on 23 Jun 2022

**HAL** is a multi-disciplinary open access archive for the deposit and dissemination of scientific research documents, whether they are published or not. The documents may come from teaching and research institutions in France or abroad, or from public or private research centers.

L'archive ouverte pluridisciplinaire **HAL**, est destinée au dépôt et à la diffusion de documents scientifiques de niveau recherche, publiés ou non, émanant des établissements d'enseignement et de recherche français ou étrangers, des laboratoires publics ou privés.

Copyright

**Key Points:**

- The Young's modulus and Poisson's ratio of sea ice are estimated from seismic noise interferometry
- Bayesian inference is applied to icequake recordings for a simultaneous inversion of the icequake position and sea ice thickness
- In comparison with our previous work, where about 50 sensors were required, the number of stations is reduced by 1 order of magnitude

**Correspondence to:**

L. Moreau,  
[ludovic.moreau@univ-grenoble-alpes.fr](mailto:ludovic.moreau@univ-grenoble-alpes.fr)

**Citation:**

Moreau, L., Weiss, J., & Marsan, D. (2020). Accurate estimations of sea-ice thickness and elastic properties from seismic noise recorded with a minimal number of geophones: from thin landfast ice to thick pack ice. *Journal of Geophysical Research: Oceans*, 125, e2020JC016492. <https://doi.org/10.1029/2020JC016492>

Received 9 JUN 2020  
 Accepted 24 OCT 2020

## Accurate Estimations of Sea-Ice Thickness and Elastic Properties From Seismic Noise Recorded With a Minimal Number of Geophones: From Thin Landfast Ice to Thick Pack Ice

Ludovic Moreau<sup>1</sup> , Jérôme Weiss<sup>1</sup>, and David Marsan<sup>2</sup> 

<sup>1</sup>Institut des Sciences de la Terre, Université Grenoble Alpes, Grenoble, France, <sup>2</sup>Institut des Sciences de la Terre, Université de Savoie Mont Blanc, Le Bourget du Lac, France

**Abstract** Despite their high potential for accurate sea ice properties estimation, seismic methods are still limited by the difficulty of access and the challenging logistics of polar environments. Conventional seismic methods generally require tens of geophones together with active seismic sources for monitoring applications. While this is not an issue for mainland environment, it is restrictive for sea ice and prevents long-term monitoring. We introduce a method to estimate sea ice thickness and elastic properties from passive recordings of the ambient seismic field with a minimal number of geophones. In comparison with our previous work (Moreau et al., 2020; <https://doi.org/10.1029/2019JC015709>) where about 50 sensors were used, the number of geophones is reduced by 1 order of magnitude, thanks to a new strategy of inversion of the passive seismic data. The method combines noise interferometry for estimating the elastic properties, with a Bayesian inversion of the dispersion in the waveforms of icequakes for inferring ice thickness, based on passive recordings from only 3–5 geophones, depending on the signal to noise ratio. We demonstrate its potential both on data recorded on thin landfast ice in Svalbard, and on data recorded on thick pack ice in the Arctic ocean.

**Plain Language Summary** Seismic methods have high potential for monitoring important properties of sea ice, such as its thickness of rigidity. Such data are essential for improving climate models. However, the use of seismic methods is limited by the difficulty of access and the challenging logistics of polar environments. It is therefore essential to reduce as much as possible the instruments required for their application. Conventional seismic methods generally require tens of geophones together with active seismic sources for monitoring applications. We introduce a method to estimate sea ice properties based on the recordings of seismic noise with only three seismic stations, and demonstrate its potential on data recorded in a frozen fjord in Svalbard, as well as on data collected on drifting sea ice in the Arctic Ocean. The method is shown to have very promising potential for long-term and accurate monitoring of the properties of sea ice.

### 1. Introduction

The propagation of seismic waves guided in sea ice has been exploited for decades to develop methods for the monitoring of the ice properties (Anderson, 1958; Marsan et al., 2012; Moreau et al., 2020; Stein et al., 1998), which are ingredients for climate and sea ice models. These methods exploit the dispersion characteristics of the guided modes that compose the wavefield. With appropriate forward modeling, an inverse problem can be defined to infer the ice thickness and elastic properties, based on a fit between the dispersion of the guided modes in the model and in the data. Such approaches are quite common, not only in geophysics, but also at the ultrasonic scale for nondestructive testing (Mitra & Gopalakrishnan, 2016) or medical acoustics (Bochud et al., 2017) applications. As far as sea ice applications are concerned, the main challenge with such monitoring methods are the in situ logistics, which require the deployment of seismic antennae with many geophones, as well as the use of active sources. Given the hostile conditions and the difficulty to access polar environments, these are considered to be the main limitations of such methods, despite their potential for accurate sea ice properties estimations. Therefore, the long-term monitoring of sea ice with seismic methods remains unlikely as long as autonomous systems with minimal deployment logistics can be used.

Thanks to rapid technological and methodological progress, these constraints are less and less limiting. For example, current technology allows miniature triaxial autonomous geophones to record continuously the seismic wavefield in polar conditions for more than 30 days, at a sampling frequency of 500 Hz. The next generation is expected to record for several months while continuously transmitting the data via satellite communication. Moreover, the need of active sources was recently made unnecessary thanks to analyses based on seismic noise interferometry (Marsan et al., 2012, 2019; Moreau et al., 2020).

In Moreau et al. (2020), a passive seismic experiment was performed to prove the concept of accurately measuring sea ice thickness and elastic properties with seismic noise. An array of 247 geophones was deployed at the surface of the frozen Van Mijen fjord in Svalbard (Norway), to record the ambient seismic field between 1 and 26 March 2019. The frequency-wavenumber dispersion curves of the guided modes propagating in the ice cover were extracted from both icequakes and the noise correlation function (NCF). These dispersion curves were inverted for sea ice thickness, Young's modulus and Poisson's ratio, yielding very accurate and robust estimates when compared with active seismic acquisitions. With this approach, the wavefield must be spatially sampled. This requires a seismic array with stations spacing that meets Nyquist's sampling criterion, with typically  $\sim 50$  stations. Although it is expected that about 20–30 stations can be sufficient to apply this technique (Moreau et al., 2017a), developing new methods able to achieve similar results with even fewer sensors is desirable to reduce in situ logistics.

We here introduce a different approach where fewer than 5 stations are sufficient to obtain accurate estimates of sea ice thickness and elastic properties. The method combines noise interferometry for estimating the elastic properties, with a Bayesian inversion of the dispersion in the waveforms of icequakes for inferring ice thickness. It takes advantage of the one-to-one relationship that exists between the time-frequency spectrum of the waveforms on the one hand, and ice thickness and propagation distance on the other hand.

The method is first applied to thin landfast ice. Based on a very rich dataset recorded in 2019 in the Van Mijen fjord, in Svalbard (Moreau et al., 2020), we demonstrate its robustness, stability, and accuracy by processing waveforms from many active sources and from icequakes (Section 3.1). Then, the method is applied to icequakes recorded on thick pack ice in the Arctic ocean in 2007 (Gascard et al., 2008; Vihma et al., 2014), indicating ice thickness values that are consistent with in situ measurements and field observations (Section 3.2).

## 2. Materials and Methods

In a layer of ice floating on water, the elastic wavefield contains at least four fundamental guided modes: the quasi-Scholte ( $QS$ ), quasi- $S_0$  ( $QS_0$ ), quasi- $A_0$  ( $QA_0$ ), and  $SH_0$  modes. When the product of the frequency by the thickness of the ice remains under 50 Hz-m, the  $QA_0$  mode is not propagative and the wavefield can be approximated with the combination of the flexural wave, the axial wave, and the shear-horizontal wave (Stein et al., 1998). These are essentially the asymptotic behavior of the guided modes, when the displacement field across the ice thickness is considered linear for the  $QS$  mode and constant for the  $QS_0$  mode (Moreau et al., 2020).

For a homogeneous waveguide, modal dispersion depends only on the product between the frequency and the thickness of the waveguide. In particular, for sea ice, the only dispersive mode under 50 Hz-m is the  $QS$  mode. The following thickness estimation procedure relies on a time-frequency analysis of this dispersion. More specifically, we minimize the misfit between the dispersion of this mode in recorded and synthetic signals. This inversion procedure is described thereafter.

### 2.1. Forward Problem: Phase-Shift-Based Propagation Model

Given a Young's modulus,  $E$ , and Poisson's ratio,  $\nu$ , the dispersion of the  $QS$  mode is characterized by a time-frequency spectrum which shape corresponds theoretically to a unique combination of ice thickness and propagation distance. A larger propagation distance results in more distorted signals with a dispersion that is specific to the ice thickness. This is illustrated in Figure 1 that shows the synthetic waveforms of the  $QS$  mode at a distance of 80 m (Figure 1a) and 250 m (Figure 1c) from the source, together with their

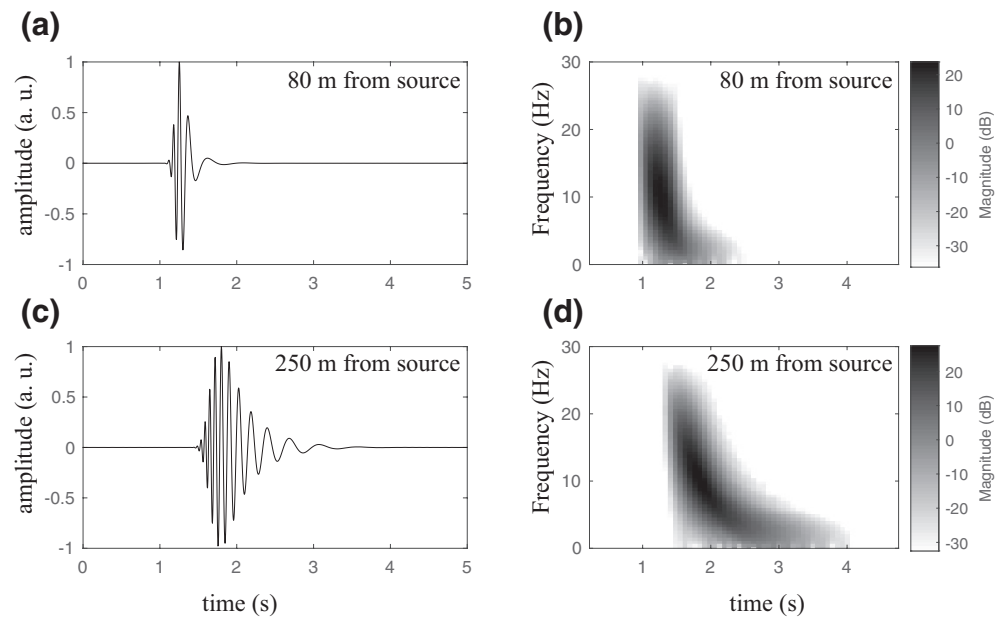


**Figure 1.** (a) Synthetic waveform of the QS mode received by a geophone located 80 m away from an impulsive source in a floating layer of ice with thickness 0.65 m. (b) Short-time Fourier transform of the waveform. (c) and (d) Same as (a) and (b) for a geophone located 250 m away from the source.

associate short-time Fourier transform (STFT), shown in Figures 1b and 1d. Here the source is assumed to produce a 1.5-cycle toneburst with a Gaussian shape, and with a center frequency of 10 Hz, which is representative of the dominant frequency observed in most of the icequakes in our data. The ice layer has a thickness  $h = 0.65$  m, Young's modulus  $E = 4$  GPa and Poisson's ratio  $\nu = 0.33$ , which is representative of the ice near the seismic array in the Van Mijenfjord (Moreau et al., 2020).

To simulate the propagation of the QS mode, we use a very basic and efficient model which applies, in the Fourier domain, the appropriate phase-shift to each frequency component of the spectrum. This phase-shift depends on the frequency and is equal to  $k(f) \times L$ , where  $k(f)$  is the wavenumber of the QS mode at frequency  $f$  and  $L$  is the propagation distance. To compute the wavenumber of the QS mode, we use the asymptotic low-frequency model introduced by Stein et al. (1998), that gives the phase velocity of a time-harmonic flexure wave in an ice layer floating on an infinite water column.

It is noteworthy that sources in the field have complex and varied mechanisms, which have an influence on wave polarization, azimuthal directivity, and signals amplitude. This results in signals that are generally quite different from a toneburst. The above-mentioned model by Stein et al. (1998) is only for calculating phase velocities, which are not dependent on source mechanisms. Hence, source mechanisms are not accounted for in this model. Moreover, the amplitude information can also be modified along the propagation, for instance if the wave encounters a lead or a ridge. Such field-dependent features cannot be accounted for either, in our basic model. Therefore, in order to mitigate their effect through the inversion procedure, the signal in the model is modified as follows:

1. generate a 1.5-cycle toneburst with a Gaussian shape and a center frequency of 10 Hz;
2. Fourier transform this signal;
3. replace the amplitude of the spectrum with that of the signal recorded at the geophone;
4. Inverse Fourier transform the modified spectrum.

This results in a pseudo-impulsive, broadband signal with a spectrum which amplitude is more representative of that from the recorded signal. This signal is then propagated between the source position and the receiver via the above-mentioned phase-shifting operation. In comparison with a nonmodified toneburst, the modified propagated waveform will have a reduced misfit with the STFT of the recorded signal.

## 2.2. Parameterization of the Problem and Cost Function

In the following, we assume that  $E$  and  $\nu$  can be estimated a priori, and we define a cost function between the data,  $\mathbf{d}$ , and the output of the model,  $\mathbf{m}(\mathbf{X})$ , based on the time-frequency analysis of the flexural wave, such that

$$f(\mathbf{d}, \mathbf{X}) = 1 - \frac{1}{N} \sum_{n=1}^N \text{corr}(\text{STFT}\{\mathbf{d}_n\}, \text{STFT}\{\mathbf{m}_n(\mathbf{X})\}) \quad (1)$$

where  $\text{corr}$  denotes the correlation coefficient between matrices  $\text{STFT}\{\mathbf{d}_n\}$  and  $\text{STFT}\{\mathbf{m}_n(\mathbf{X})\}$ .  $\mathbf{d}_n$  is the temporal signal recorded on the vertical channel at station  $n$  ( $n = 1, 2, \dots, N$ ) when an impulsive seismic source is activated, for example, an icequake.  $\mathbf{m}_n(\mathbf{X})$  is the temporal signal simulated at station  $n$ , based on the input parameters,  $\mathbf{X}$ . The parameters are representative of the wave propagation problem:

1. source latitude;
2. source longitude;
3. ice thickness,  $h$ ;
4. a time-shifting parameter,  $\Delta t$ , that accounts for the unknown activation time of the source during the recordings. The aim of this parameter is to “align” the simulated and recorded waveforms. It is the same for all stations.

This problem is very well-constrained because there is a one-to-one relationship between the model parameters and the global minimum of the cost function. Hence in theory it should be possible to estimate sea ice thickness based on a single signal recorded by a unique seismic station. In practice, however, this can hardly be achieved because the waveforms are corrupted by ice heterogeneity, thickness variations, the presence of a snow layer, anisotropy of elastic properties, etc. Nonetheless, the impact of these uncertainties can be mitigated by including data from a few more seismic stations. This significantly improves source localization, which simultaneously also improves thickness estimation. The resulting inferred ice thickness corresponds to an average over all the direct paths between the source and the stations.

## 2.3. Inverse Problem

To solve the inverse problem, we proceed with Bayesian inference, which provides an ensemble of solutions that fit the data with an acceptable level of likelihood, given the data uncertainty. This ensemble of solutions is represented by the posterior distribution of the model parameters, such that

$$P(\mathbf{X} | \mathbf{d}) = \frac{P(\mathbf{d} | \mathbf{X})P(\mathbf{X})}{P(\mathbf{d})}. \quad (2)$$

$P(\mathbf{X} | \mathbf{d})$  is the likelihood function,  $P(\mathbf{X})$  is the prior distribution and  $P(\mathbf{d})$  is the marginal likelihood function, or the model evidence. The posterior distribution expresses the conditional probability of the parameter values based on evidence from measurements, expressed by the likelihood function, and from prior assumptions, expressed by the prior distribution.

The Markov Chain Monte Carlo (MCMC) algorithm is one of several methods that can be used to evaluate the Bayesian posterior distribution by realizing a Markov chain in the parameter search space. This random walk satisfies the ergodic theorem, which allows the algorithm to converge toward a stationary state that approximates the probability density function (PDF) of the parameters (Andrieu & Moulines, 2006). A recurrent problem in Bayesian inference is the difficulty to calculate the marginal likelihood, which is essentially a normalization factor. However, because it is the same for all probabilities, its determination is not necessary in practice, since it can be canceled by comparing ratios of probabilities rather than absolute probabilities. This is one of the motivations for using methods based on stochastic sampling such as MCMC.

In the present problem, it is assumed that measurement errors are uncorrelated and random, and thus they can be modeled by a normal distribution. A zero-mean Gaussian likelihood function with variance  $\sigma^2$  is therefore prescribed:

$$P(\mathbf{d} | \mathbf{X}) = \exp\left(-\frac{(f(\mathbf{d}, \mathbf{X}))^2}{2\sigma^2}\right), \quad (3)$$

where  $\sigma^2$  is the variance associated to the measurement errors. This is a typical likelihood function used in many data fitting problems (Tarantola, 2005). Moreover, it is also assumed for the prior distribution, that the model parameters have equal probability over a finite range of values:

1. The position of sources, which mainly originate from leads, ridges, or the shore line, is within a distance of 2 km around the center of the arrays.
2. Ice thickness is comprised between 0.1 and 5 m.
3. The phase-shift adjustment parameter is between  $-t_{\max}$  and  $+t_{\max}$ , where  $t_{\max}$  is the size of the time window where the signals to invert are recorded.

MCMC methods generally require a burn-in phase before reaching the posterior distribution. For improved convergence, we precede the MCMC algorithm by a simulated annealing (SA) global optimization. The number of iterations is set to 10,000 in the SA and to 100,000 in the MCMC algorithm. To approximate the PDF of the parameters, we sample 1,000 candidates from the posterior distribution of each parameter. Thanks to the ergodic theorem, the mean of the PDF returns the expectation of the parameters, which is also considered here to be the estimated value, because the PDF should be centered around the zone with the highest probability in the parameter space. Another interest of the MCMC algorithm is to provide a confidence in the solution, based on the shape of the PDF.

### 3. Results

#### 3.1. Landfast Ice in the Van Mijen Fjord in Svalbard

The data processed in this section were recorded in the Van Mijen fjord near Sveagruva, in Svalbard (Moreau et al., 2020). Figure 2a shows the location of the deployment in the fjord. The array is located near Sveagruva in a part of the fjord that is surrounded by a moraine and connected to the fjord by a channel (Figure 2b). The array contains a total of 247 FairFieldNodal Zland geophones (flat frequency response down to the cut-off frequency of 10 Hz for 1C instruments and 5 Hz for 3C instruments, and an attenuation of  $-20$  dB per decade below), as shown in red and blue in Figure 2c.

##### 3.1.1. Elastic Properties of the Ice

Prior to applying the inversion procedure to the data, the Young's modulus and Poisson's ratio of the ice must be determined. To this end, we evaluate the velocity of the guided  $QS_0$  and  $SH_0$  modes from the NCF. In passive seismology, the NCF is calculated by correlating the ambient seismic noise (or ambient seismic field) recorded between pairs of stations. It can be shown that it converges toward the impulse response, or Green's function, of the medium (Sabra et al., 2005; Shapiro & Campillo, 2004). As shown in Moreau et al. (2020), this approach can be applied to seismic noise recorded on sea ice to recover the Green's function of the wavefield propagating between the stations of a seismic array.

When the product of the wavefield by the thickness of the ice remains low, typically up to 200 Hz·m, the  $QS_0$  and  $SH_0$  modes guided in the ice produce a displacement that is dominant on the horizontal components of the wavefield. Hence, we compute the NCF from ambient noise recorded on the horizontal channels of the five geophones shown as squares in Figure 2c. The noise was recorded between 0h00 and 8h00 on March 5, 2019. Recordings were first truncated in 5 mn-long time windows and spectral whitening was applied in the [1–20] Hz frequency band. The cross correlations were then calculated between each station pair, for all 96 time windows. To obtain the final NCF, the filter introduced in Moreau et al. (2017b) was applied to each set of cross correlations, which were finally stacked.

These NCF are shown in Figure 3 for the 10 combinations of station pairs as a function of the distance between the stations. They indicate an average velocity of 2,170 m/s for the  $QS_0$  mode and 1,235 m/s for the  $SH_0$  mode. These can be related to Young's modulus and Poisson's ratio such that (Stein et al., 1998):

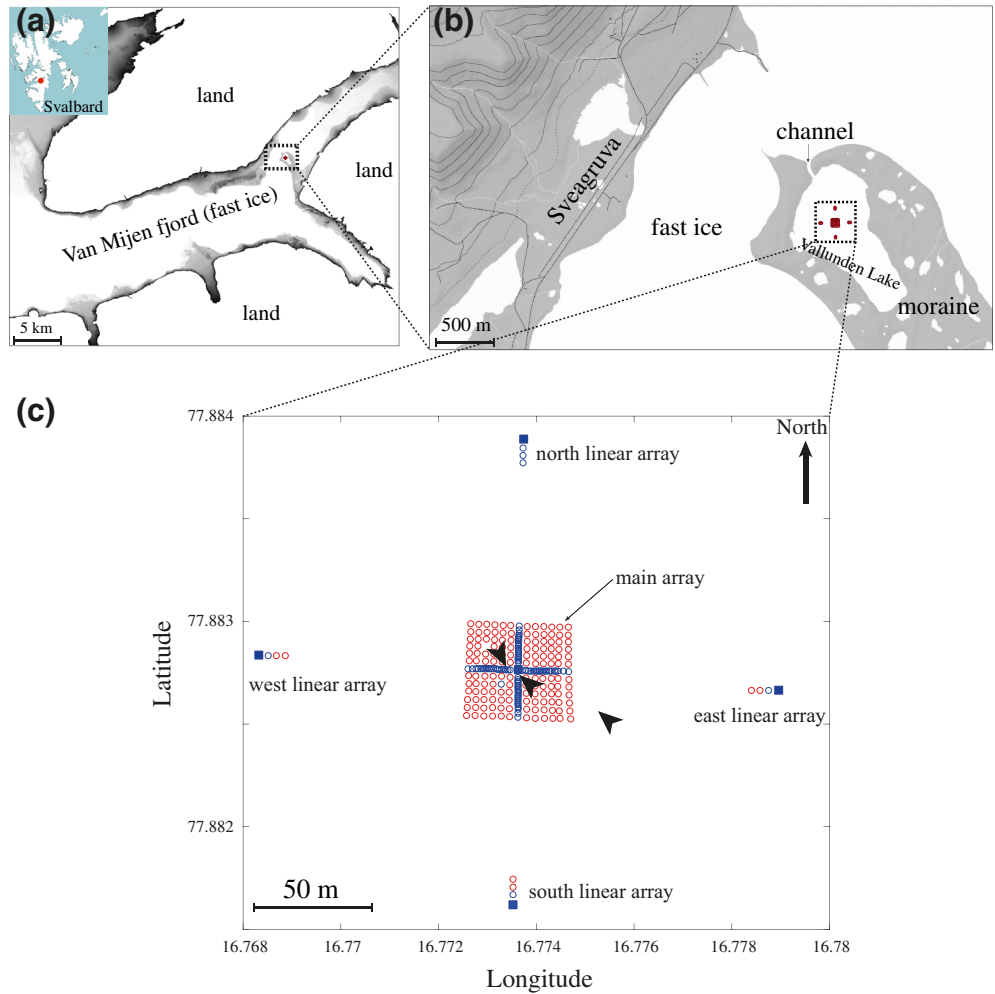


**Figure 2.** (a) Location of the seismic array in the Van Mijen fjord near Sveagrøva (Svalbard), with (b) a zoom around the array area near Vallunden Lake, a part of the fjord that is surrounded by a moraine and connected to the fjord by a channel. The gray scale shows land whose altitude is less than 25 m. All land above 25 m is shown in white to emphasize the shore line. (c) The 247 stations of the array, including the main central array, and the four linear arrays to the north, east, south, and west. Red circles are for 1C stations and blue circles for 3C stations. The five blue squares indicate the stations used in Section 3.1 to calculate the NCF. The large arrowheads indicate the positions of ice thickness measurements.

$$\nu = 1 - 2 \left( \frac{c_{QS} H_0}{c_{QS_0}} \right)^2, \text{ and } E = \rho \times (c_{QS_0})^2 (1 - \nu^2). \quad (4)$$

This gives  $E = 3.8$  GPa and  $\nu = 0.35$ , which is consistent with the values reported in Moreau et al. (2020):  $E = 3.9 \pm 0.2$  GPa and  $\nu = 0.34 \pm 0.02$ , which were estimated from a frequency-wavenumber analysis based on the recordings of 52 geophones. The density is set to  $900 \text{ kg/m}^3$ , a common value for sea ice. From a rheological point of view, it would be of interest to monitor the evolution of these mechanical properties between 1 and 26 March. Preliminary results indicate that Poisson's ratio keeps a conservative value between 0.32 and 0.33, and Young's modulus remains stable between 3.8 and 4.5 GPa. However, this is out of the scope of this paper and is left for separate study.

Next, we apply the inversion method to both active sources (jumps from 1-m height onto the ice), and passive sources (icequakes). The active sources are ideal for a preliminary investigation of the accuracy of the inverted parameters, because they produce signals with a better signal to noise ratio, and also because

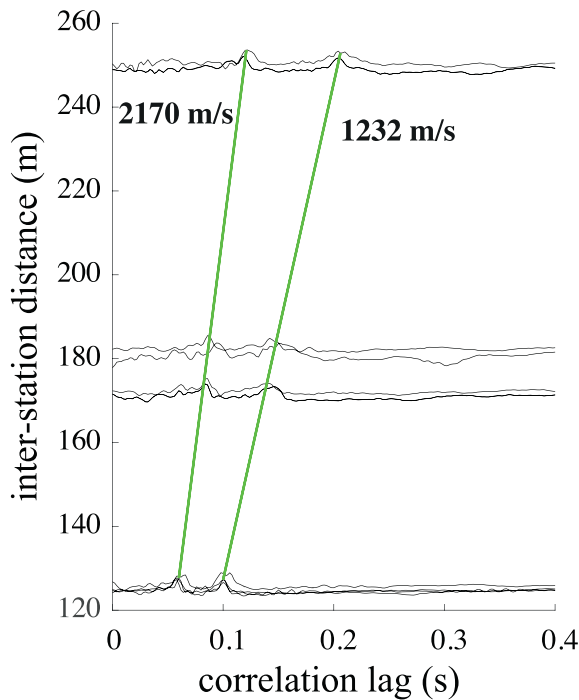


**Figure 3.** NCF from 8 h of seismic noise recorded between 0h00 and 8h00 on March 5, 2019 in the Van Mijen Fjord, at the stations of the array shown as blue squares in Figure 2c, versus the distance between the stations. The green lines indicate the arrival time of the  $QS_0$  and  $SH_0$  modes, which propagate at a velocity of 2,170 and 1,232 m/s, respectively.

exhibits an increasing arrival time, there are also patterns where arrival times are not increasing monotonically, which does not happen when choosing stations that are all in a same line. This is typical of an apparent anisotropy.

### 3.1.2.1. Robustness of the Inversion

In order to check the robustness of our inversion procedure with regard to these uncertainties, we performed 30 successive inversions of the same source (jump near the northernmost geophone) at two different dates on 1 and 26 March 2019. Each inversion was performed with a different set of geophones that were randomly selected amongst the 247 available. The results of the inversions are given in Table 1 when using 3 and 5 stations for the inversions. These results show that the method is very robust to the apparent anisotropy, with accurate location of the sources, and thickness estimates with a standard deviation of less than 6.5 cm. It is also noteworthy that when using 3 stations, we identified two cases where the position of the source was less constrained. This occurred in cases where the three stations were close to one another (less than 15 m away), thus creating artificial far-field conditions which prevent the azimuthal direction to be constrained. Such configurations were not encountered with 5 stations.

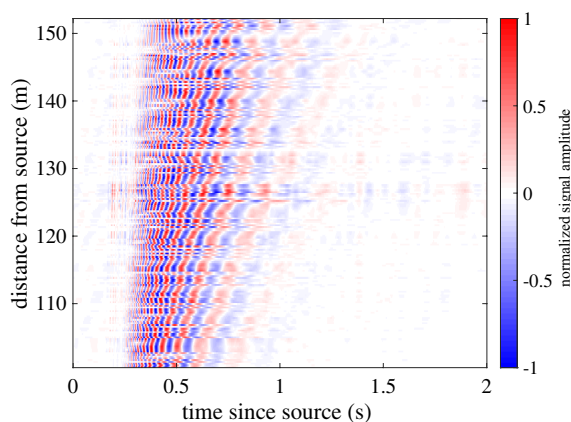


**Figure 4.** Normalized signals received at all stations of the main array versus the distance from an impulsive source located in the north linear array. Depending on propagation direction, the moveout of the waveforms is not increasing monotonically, revealing an apparent anisotropy of the wave propagation.

their exact location is known. We present inversions for these two types of sources, based on signals recorded with 3 and 5 stations.

### 3.1.2. Inversions of Active Sources for Ice Thickness

On 1 and 26 March 2019, a series of active acquisitions were performed by jumping directly onto the ice from a 1-m height, near the linear arrays to the north, east, south, and west of the main array (Figure 2c). In total, 16 jumps were performed on both dates, each at a distance of about 0.5 m from the geophones in the linear arrays. Signals were extracted from the continuous recordings in a 5 s time window following the jumps. We refer the reader interested in the exact jumps time to Moreau et al. (2020), where they are all listed. The inversion relies on a forward model that is valid when the product of the frequency by the thickness of the ice remains under 50 Hz·m. Since the ice thickness in the fjord was less than 1 m, the extracted signals were band-pass filtered in the (1–50) Hz frequency band.

Although the landfast ice in the fjord is more regular than drifting ice in the open sea, it exhibits significant heterogeneities of mechanical properties through the thickness, as well as local thickness variations by up to 20 cm (Moreau et al., 2020). These heterogeneities and thickness variations induce an apparent anisotropy in the propagation of the guided waves. For example, Figure 4 shows the waveforms recorded at the main array in the 2 s following a jump at the north linear array. The waveforms are sorted with respect to the increasing distance between the stations and the jump location. The 231 stations of the main array are distributed on a square grid. Hence this sorting implies that from one waveform to the next, the propagation direction can be very different ( $\pm 15^\circ$ ) while the propagation distance is almost the same. Although the overall moveout

is almost the same. Although the overall moveout

is almost the same. Although the overall moveout

### 3.1.2.1. Robustness of the Inversion

In order to check the robustness of our inversion procedure with regard to these uncertainties, we performed 30 successive inversions of the same source (jump near the northernmost geophone) at two different dates on 1 and 26 March 2019. Each inversion was performed with a different set of geophones that were randomly selected amongst the 247 available. The results of the inversions are given in Table 1 when using 3 and 5 stations for the inversions. These results show that the method is very robust to the apparent anisotropy, with accurate location of the sources, and thickness estimates with a standard deviation of less than 6.5 cm. It is also noteworthy that when using 3 stations, we identified two cases where the position of the source was less constrained. This occurred in cases where the three stations were close to one another (less than 15 m away), thus creating artificial far-field conditions which prevent the azimuthal direction to be constrained. Such configurations were not encountered with 5 stations.

### Stability of the Inversion

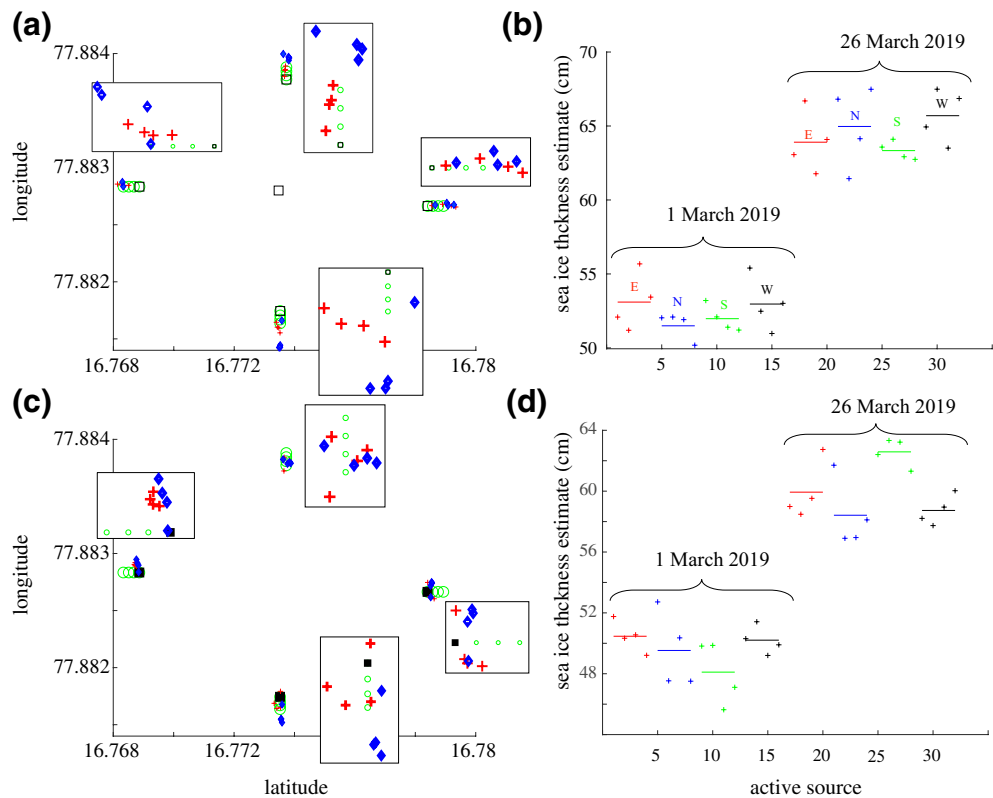
Next, we also check the stability of the thickness estimations when applied to sources located nearby each other. To this end, once again the four sources at each linear array are used on both dates. Inversions are performed with 3 or 5 stations (Figure 5). When using 5 stations, sources to the north, east, south, and west are located very accurately, as shown in



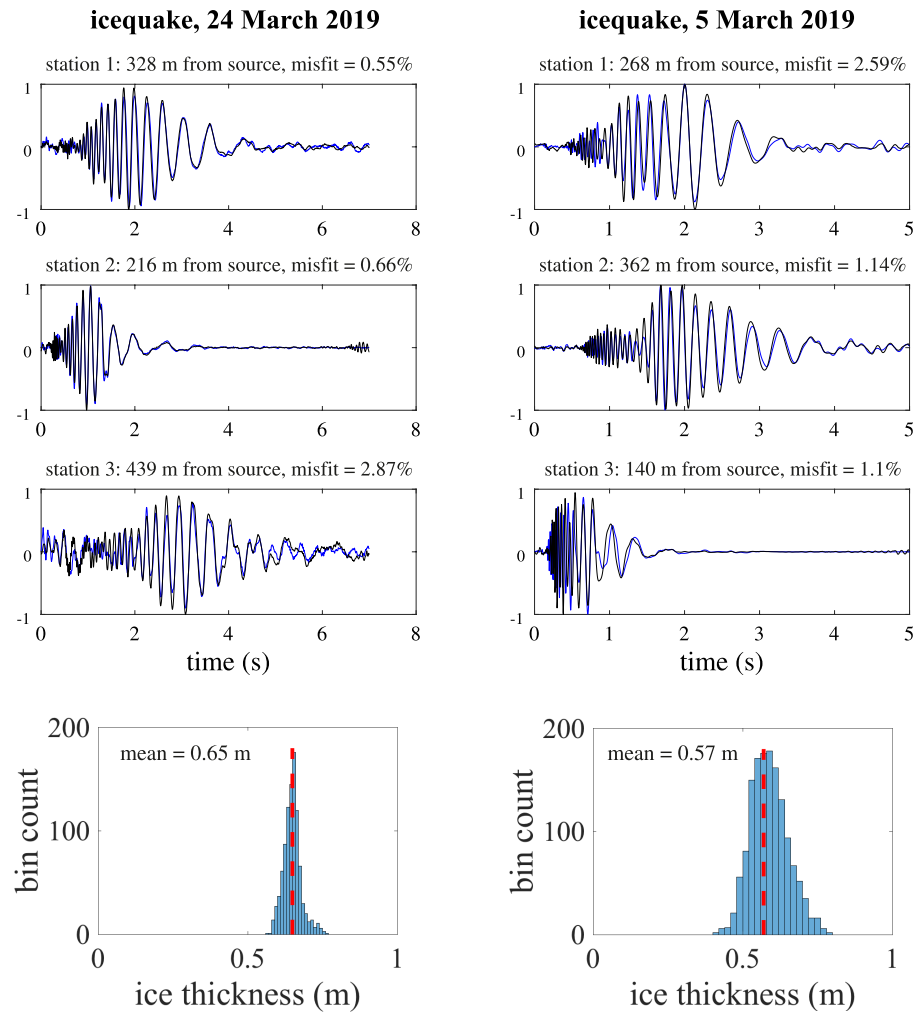
Date	March 1, 2019	March 1, 2019	March 26, 2019	March 26, 2019
Number of stations for inversion	5 stations	3 stations	5 stations	3 stations
Average error on source position	4.6 m	5.2 m	6.5 m	6.3 m
Ice thickness estimation	50 ± 3 cm	52 ± 4.5 cm	67 ± 6.5 cm	68 ± 6.6 cm

Figure 5a. At both dates, the ice thickness estimates are all within a 4 cm range for each of the four source areas (Figure 5b). When using 3 stations, results have comparable source location accuracies. In terms of ice thickness estimation, the values remain within a range of 6 cm, which is slightly larger than with 5 stations, but still very accurate, especially when considering that part of the variability is most likely due to the direction of propagation, and thus to actual spatial variations of thickness. Overall, the inversion can therefore be considered very stable since estimations from sources located in the same area give very similar values.

Note the increase of thickness between 1 and 26 March. This was also observed in the field from ice drillings and ground penetrating radar acquisitions, which indicated an increase of 10–15 cm. Moreover, the thickness estimates are consistent with the values found when applying the method introduced in Moreau et al. (2020). This method is based on a simultaneous inversion of the frequency-wavenumber spectrum of the  $QS$ ,  $QS_0$ , and  $SH_0$  modes. This gave  $h = 54$  cm with a standard deviation of 3 cm on 1 March, and  $h = 74$  cm with a standard deviation of 5 cm on 26 March. The slight differences between the two methods are due to the fact that, on the one hand, the inversion in Moreau et al. (2020) averages thickness variations



**Figure 5.** (a) Inverted position of all active sources on 1 March (+) and 26 March (◆) 2019. Green circles represent the sources positions and black squares the stations used for the inversions. The four boxes show a zoom of the localized sources near each linear array. (b) Ice thickness estimates from these inversions. (c) and (d) Same as (a) and (b) with 3 stations only.



**Figure 6.** Top: waveforms of the icequakes recorded in the Van Mijen fjord (black) and the corresponding synthetic waveforms (blue), resulting from the inversion with 3 stations ( $S_1$ ,  $S_2$  and  $S_3$ ; see Figure 7). Bottom: PDF of the ice thickness, with the mean value shown as dashed line.

along a short line of 50 stations ( $\sim 50$  m) via a spatial Fourier transform. On the other hand, the present method averages wave propagation on larger propagation paths ( $\sim 250$  m), each with very different directions between the source and the stations.

### 3.1.3. Inversions of Icequakes for Ice Thickness

The main objective is to achieve accurate thickness estimations from passive data only, so that long-term monitoring is made possible without the need of human intervention in the field, other than the deployment of the geophones. Therefore, the method is now applied to icequakes recorded on 5 and 24 March 2019. We attribute these icequakes to the presence of cracks that were observed in the field all along the shore line of the fjord. They are most likely produced by the mechanical stress induced by tidal forcing, and they were either closed or partially open, depending on the tidal phase. The waveforms of these icequakes are shown in Figure 6 for three stations,  $S_1$ ,  $S_2$ , and  $S_3$  (Figure 7), together with the corresponding synthetic waveforms resulting from the inversion with these stations. The average misfit after inversion is of the order of 1% for both icequakes, indicating that the data can be explained remarkably well with the simple forward model based on four parameters only.

The results of the inversions are shown in Figure 7, when using 5 stations (Figure 7a) or 3 stations (Figure 7b), both indicating identical locations of the icequakes. The PDF is slightly more dispersed when only

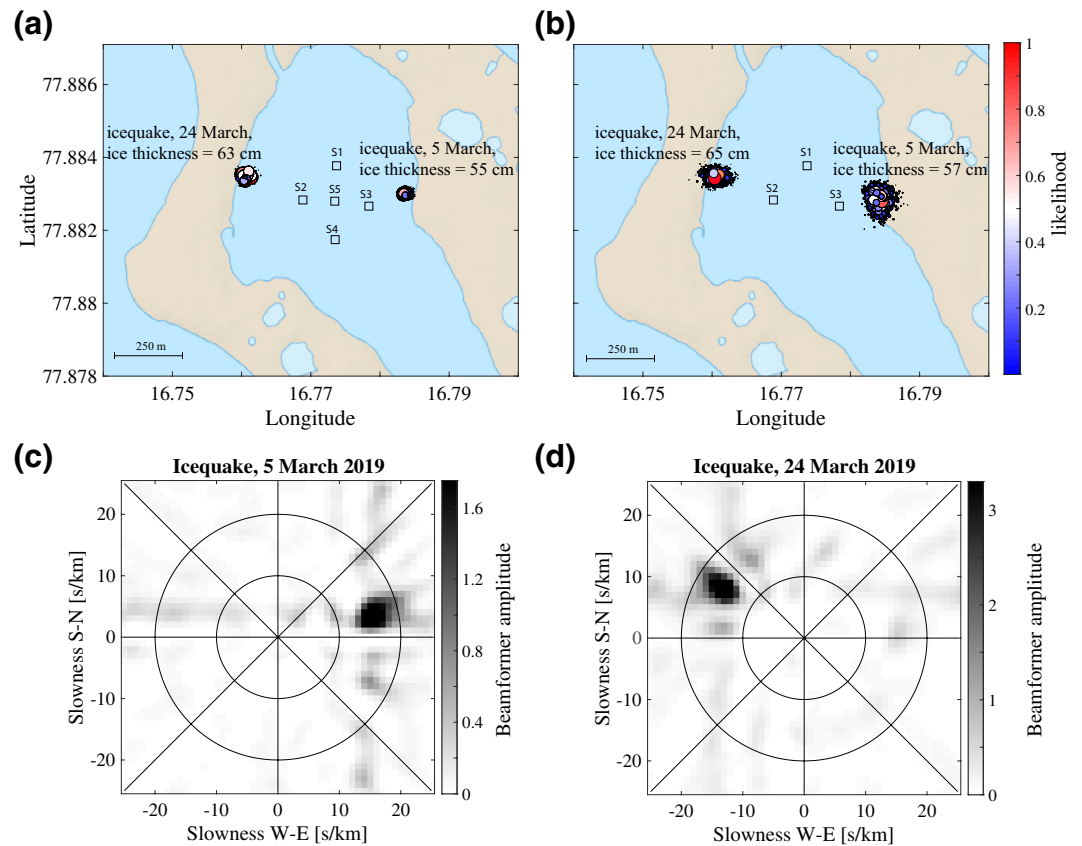


**Figure 7.** Top: Map showing the result of inversions for icequakes recorded at the Van Mijen fjord. The diameter and color of the circles are proportional to the likelihood in the posterior distribution of the parameters. The squares indicate the stations used for the inversions. Inversion of the icequakes was performed with (a) 5 stations and (b) 3 stations. Stations are labeled  $S_i$ ,  $i = 1, 2, \dots, 5$ . Bottom: Slowness versus azimuth linear beamforming of the icequakes recorded on (c) 5 March and (d) 24 March. The beamforming was computed in the 7–9 Hz frequency band, using the 231 stations of the main array. Some slight aliasing is visible.

3 stations are used. This was expected, since the more stations for the inversion, the better constrained the location parameters. The icequake on March 5 is located along the shore to the east of the array, and that on March 24 is located along the shore to the west of the array. This is consistent with the directions found from linear beamforming of the data using all stations of the main seismic array. This beamforming is shown in Figures 7c and 7d as slowness of the waveforms versus azimuthal direction. Regarding the thickness, on March 5 the estimated value is 55 cm with a standard deviation of 2.5 cm in the PDF when using 5 stations, and 57 cm with a standard deviation of 3 cm in the PDF when using 3 stations. On March 24, the estimated thickness is 63 cm with a standard deviation of 2.7 cm in the PDF when using 5 stations, and 65 cm with a standard deviation of 3 cm in the PDF when using 3 stations. These values are consistent with those found when using active sources, as well as with estimations from the same icequakes when applying the method introduced in Moreau et al. (2020), based on an inversion of the wavenumbers of the modes.

### 3.2. Pack Ice Within the Arctic Ocean

The seismic data analyzed in this section were already described in Marsan et al. (2011): a seismic network was deployed in April 2007 as part of the measurement campaign at the Tara drifting station operating in the framework of the Developing Arctic Modeling and Observing Capabilities for Long-term Environmental Studies (DAMOCLES) project (Gascard et al., 2008). Figure 8a shows a part of this network made of four seismic antennae labeled Tromso, Paris, Tartu, and Helsinki. Each antenna contains four short-period (1 Hz) vertical seismometers and one broadband Guralp CMG-3ESPC seismometers, installed in a

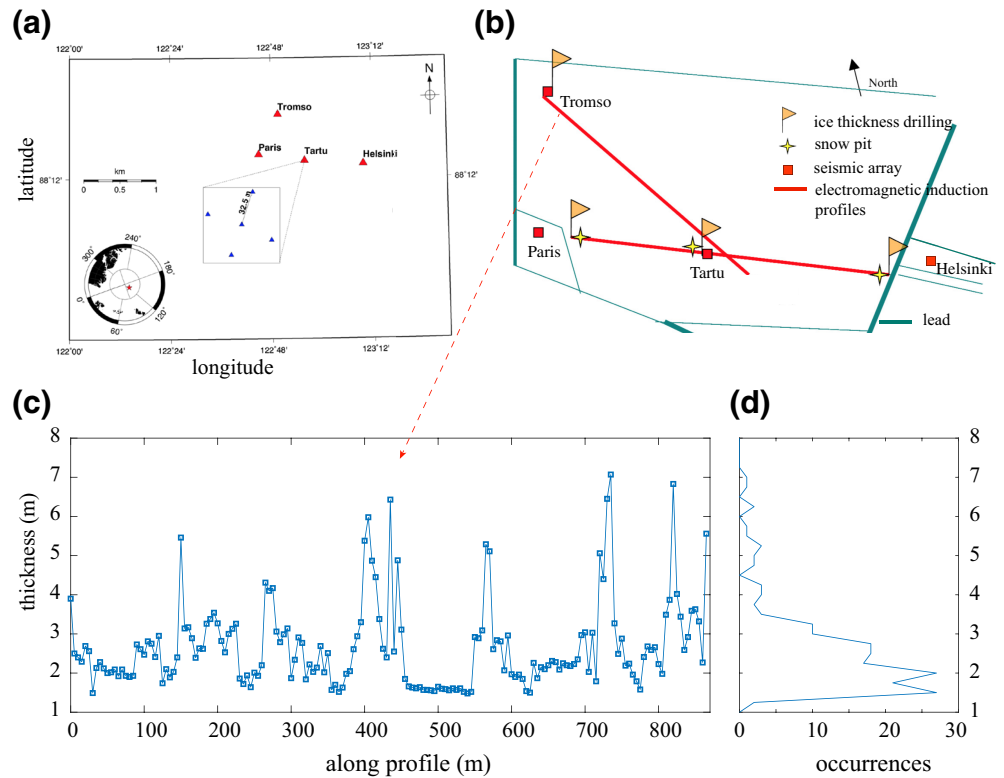


**Figure 8.** (a) Sketch of the four seismic antennae Tromso, Paris, Tartu, and Helsinki, installed at the Tara ice station. The inset shows the geometry of one array, with typical intersensor distance. (b) Approximate map showing the situation in the field, with the position of the antennae relative to the leads, as reported by the Tara’s onboard crew. (c) Ice thickness profile from drilled holes and electromagnetic induction between stations Tromso and Tartu. (d) Histogram of the thickness values.

diamond-shaped geometry with the triaxial seismometer in the center. Figure 8b shows an approximate map of the situation in the field, with many leads around the four antennae, as well as the ice drilling and electromagnetic sounding positions relative to the antennae. The corresponding thickness profile between antennae Tromso and Tartu are shown in Figure 8c, together with an histogram of thickness values (Figure 8d), which indicates that the average thickness of the level ice is about 2 m.

For our analyses, we use 1 h of continuous recordings on May 1, 2007 between 0:00 and 1:00, at antenna Helsinki (Figures 8a and 8b). One of these recordings is shown in Figure 9a, with a zoom between 0:30:30 and 0:36:00 (Figure 9b) and the corresponding spectrogram (Figure 9c). Hundreds of icequakes with energy up to 25 Hz are visible. In order to satisfy the validity criterion of the forward model, signals are low-pass filtered under 10 Hz. This allows thicknesses up to ~5 m to be tested while keeping frequency-thickness values under the upper limit of 50 Hz·m.

### 3.2.1. Elastic Properties of the Ice

Because only one station of the Helsinki antenna is a 3C instrument, the method used in Section 3.1 to evaluate Young’s modulus and Poisson’s ratio from noise interferometry is not possible here. We tried to exploit the horizontal channels of this station by including, in the cost function, the arrival times of the  $QS_0$  and  $SH_0$  modes. This would allow the velocity of the modes to be evaluated, based on the propagation time and the distance from the source, which could be used in turn for a joint inversion of ice thickness and elastic properties. However, this approach was not conclusive due to poor SNR in the data, which prevented the arrival times of these modes to be picked accurately. A potential solution consists in looking for icequakes originating from identical sources (also known as repeaters), via template matching methods.

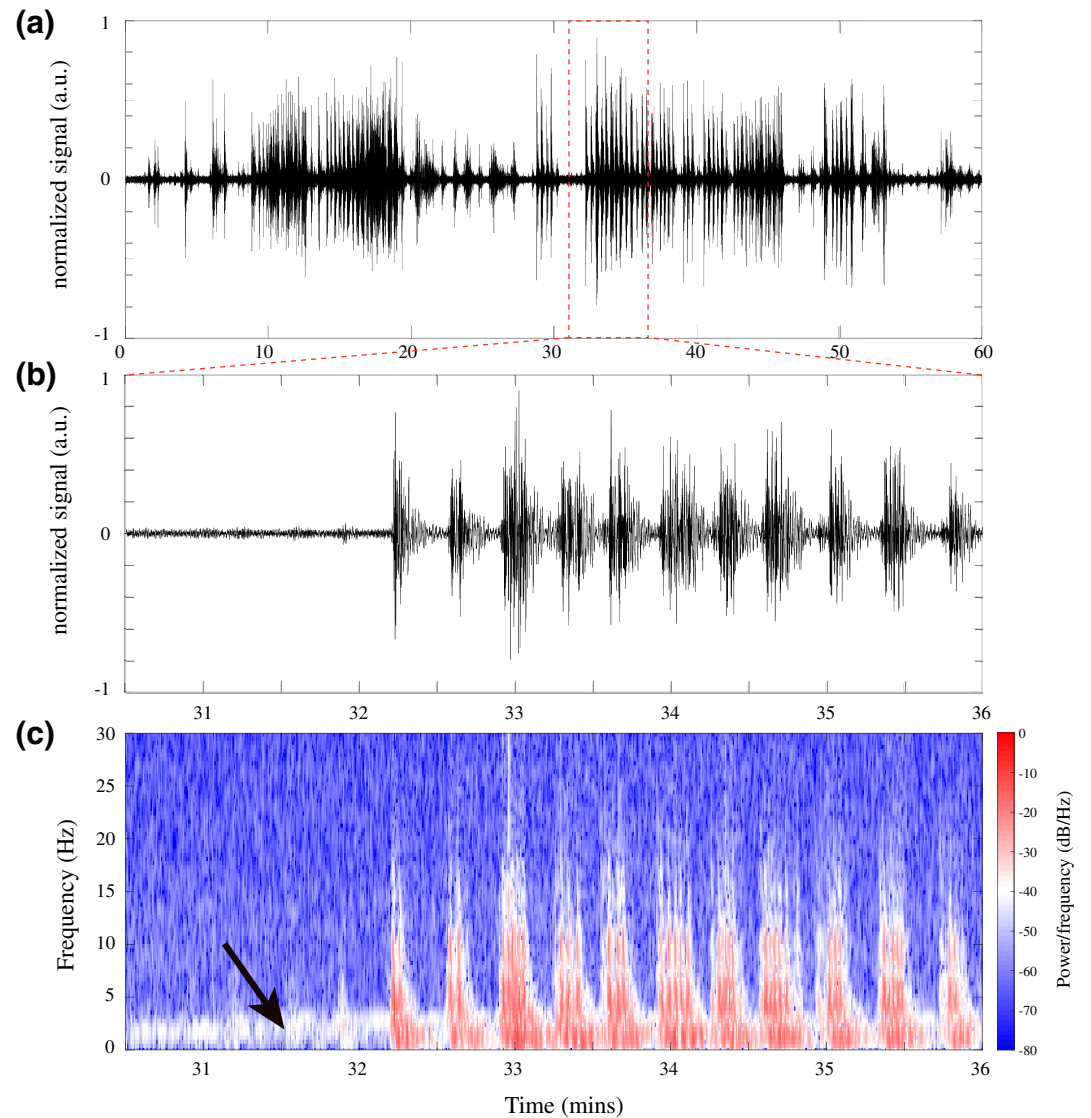


**Figure 9.** (a) One hour of seismic recording at one station of the HELSINKI antenna. (b) Zoom between 0:30:30 and 0:36:00 and (c) the corresponding short-time Fourier transform. The black arrow indicates a systematic seismic noise with energy between 0.5 and 3 Hz.

Stacking those waveforms could help tackle the SNR issue. However, the goal here is to demonstrate the potential of the inversion method when applied to a dataset acquired with the appropriate instruments, and there is no doubt that the elastic properties of the ice could be determined from the NCF, for example, if the same geophones as those used on landfast ice had been used too. Hence, such ad hoc solutions are not investigated further here, since they are out of the scope of this paper.

For thick pack ice, reports in the literature give Young's moduli that vary between 6.1 and 8.6 GPa, while values for Poisson's ratio are more conservative around  $\nu = 0.33$  (Hunkins, 1960; Stein et al., 1998). In absence of in situ evaluations of the elastic properties, we use  $E = 7.2$  GPa and  $\nu = 0.33$ , following the recommendation in Marsan et al. (2012), and the density is set to  $900 \text{ kg/m}^3$ . Of course, choosing a different value of Young's modulus would change the value of the inferred ice thickness. However, this change would not be significant because the ice thickness parameter is much more constrained by the curvature of the STFT than it is by Young's modulus. Nonetheless, further investigations are required to quantitatively evaluate

this sensitivity. This is left for a separate study, as this represents a considerable amount of inversions and analyses that are out of the scope of this paper.

### 3.2.2. Inversion of Icequakes for Ice Thickness

The vast majority of the recorded icequakes are not resolved in time, as shown in Figure 9b, where one can see that the waveforms are partly superposed. This prevents a clear dispersion to be extracted from the time-frequency spectrum (Figure 9c). The waveforms are also much noisier than those recorded in the Van Mijen fjord. We suggest that this is due to (i) instrumentation issues, because SNR varies significantly between the stations, and to (ii) a noisier environment, as shown in Figure 9c where a low-frequency seismic noise with energy between 0.5 and 3 Hz is always present. Unfortunately, this is a frequency band where part of the useful dispersion information is present as well. This reduces the amount of icequakes suitable for an inversion to less than 1%. Yet, this should not be considered a fundamental problem, given the thousands of icequakes that trigger every day. Moreover, the thickness profile shown in Figure 8c indicates significant local variations between 1.6 and 7 m, due to deformed ice and pressure ridges (Haas et al., 2011). Such large variations likely modify the seismic wave propagation and cause scattering. With all the above-mentioned difficulties, this dataset represents the main challenge for our proof of concept.

To select icequakes suitable for an inversion, the following heuristic criteria were used:

1. The waveforms are clearly resolved in time and well-separated from those of other icequakes.
2. The SNR in the time-frequency spectrum allows the dispersion to be quantified between 0.5 and 20 Hz.

Based on these criteria, three icequakes were selected. The waveforms of two of these icequakes are shown in Figure 10, together with the corresponding synthetic waveforms resulting from the inversion with 5 stations. The average misfit after inversion is of the order of 5%–10%. This indicates that the data can be explained reasonably well with the forward model. Figure 11 shows the corresponding inversions, performed with 5 stations (Figure 11a) and less (Figure 11b). The posterior distributions are shown in terms of the icequakes position relative to the array. They all indicate that the icequakes originate from the main lead located to the west of the array. With 5 stations, the estimated thickness was:

1. 2.02 m for the icequake recorded at 0:02:06 with a standard deviation of 33 cm in the PDF;
2. 2.06 m for the icequake recorded at 0:02:19 with a standard deviation of 32 cm in the PDF;
3. 2.04 m for the icequake recorded at 0:28:47 with a standard deviation of 35 cm in the PDF. Note the non-Gaussian shape of the PDF. This suggests a local minimum, in the cost function, that is associated to a thickness with relatively high likelihood around 2.5 m.

And with less than 5 stations:

1. the inversion for the icequake recorded at 0:02:06 was not conclusive;
2. 2.08 m for the icequake recorded at 0:02:19 with a standard deviation of 37 cm in the PDF, with 4 stations;
3. 2.03 m for the icequake recorded at 0:28:47 with a standard deviation of 39 cm in the PDF, with 3 stations, although the icequake was not located exactly at the same position as when using 5 stations. Moreover, the PDF of the position parameters exhibits a wider spread. This is most likely a consequence of poor SNR combined with fewer stations used for the inversion.

In absence of thickness measurements around the array, we cannot give a definitive answer regarding the accuracy of these estimates. However, they are consistent with the measurements shown in Figures 9b and 9c which indicate an average thickness of ~2 m for the level ice, west of the main lead. These results are very encouraging, since we demonstrate that, despite poor SNR and significant local thickness variations that scatter wave propagation, icequakes can be located and ice thickness inferred with very good confidence. The standard deviation in the PDF are of the order of 30 cm, which indicates that the confidence in the solution is not as good as for the estimations from the previous dataset. This is a consequence of the larger misfit value (~5%–10% instead of ~1%). We are confident that this misfit could be reduced by (i) using instruments of the latest generation (for example, those used on landfast ice), and (ii) using a forward model able to account for the local variations in ice properties, such as a finite element model, but at the cost of significantly increased computational resources. However, we suggest that the actual standard deviation

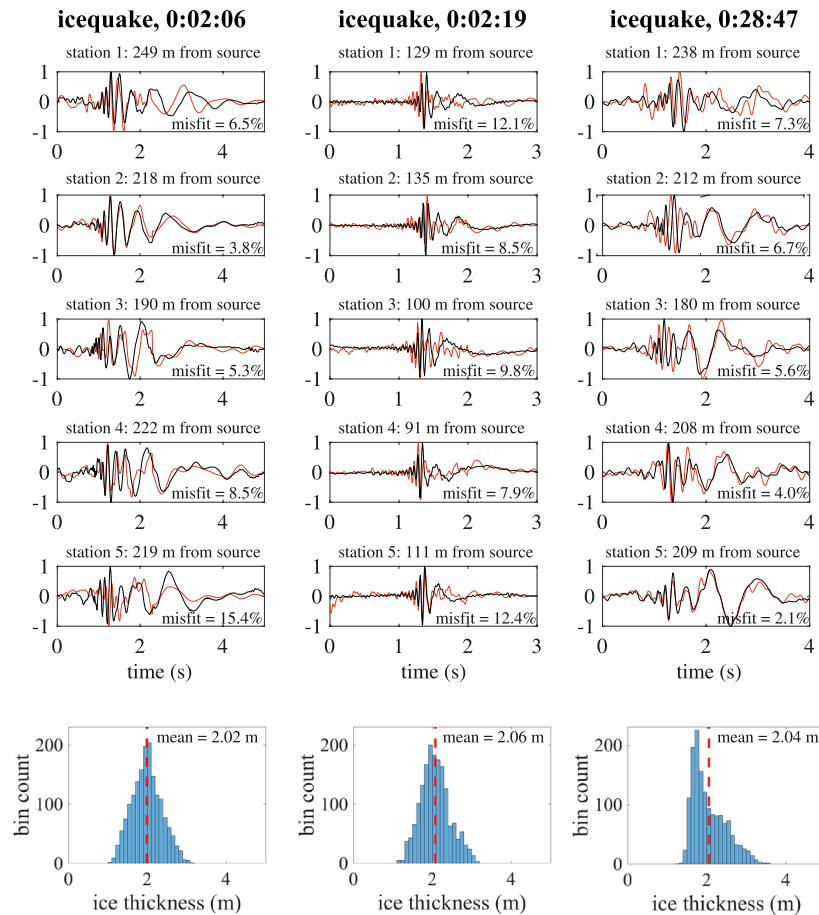


**Figure 10.** Top: Waveforms of the icequakes recorded on pack ice (black) and the corresponding synthetic waveforms (red), resulting from the inversion with 5 stations. Bottom: PDF of the ice thickness with the mean value shown as dashed line.

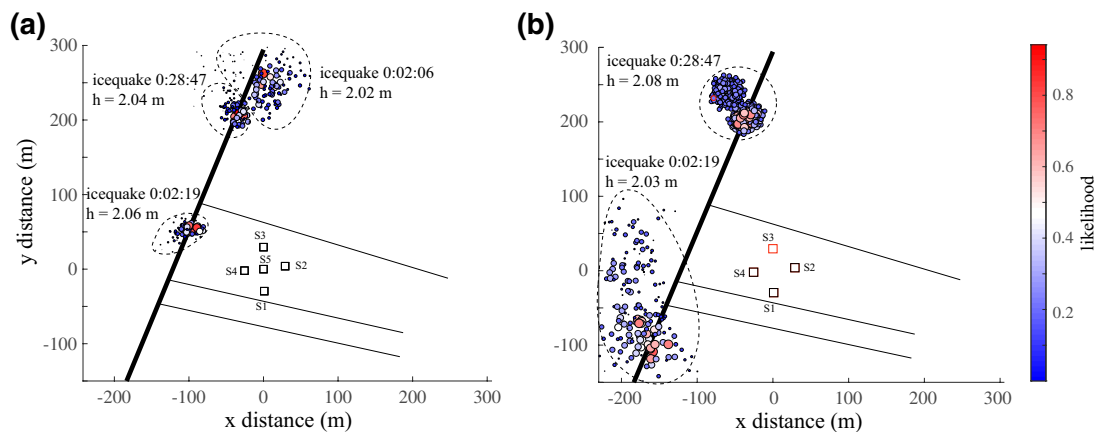


**Figure 11.** Map showing the result of inversions for icequakes recorded on drifting sea ice at the Helsinki antenna. The diameter and color of the circles are proportional to the likelihood in the posterior distribution of the parameters. The squares indicate the stations used for the inversions. Solid lines show the approximative position of the leads relative to the stations. (a) Inversion of three icequakes with 5 stations. (b) Inversion of the icequake at (i) 0:02:19 with 3 stations (black squares), and (ii) 0:28:47 with 4 stations (black and red squares). The black dashed curves delimit the PDF of the icequakes position. The dashed curves separate the PDF of icequakes position.

of the ice thickness estimation is much less than that in the PDF, since all inferred values remain within a 6 cm margin.

#### 4. Concluding Remarks

A method was introduced to estimate the elastic properties of sea ice from seismic noise interferometry, as well as the ice thickness from the time-frequency dispersion of the flexural wave. This approach only requires passive recordings of seismic noise on 3–5 triaxial seismic stations (depending on SNR), to provide accurate and robust estimations of sea ice properties, while simultaneously relocating the icequakes. In thin landfast ice, we found an ice thickness between ~55 cm at the beginning of March and ~65 cm at the end of March, with a standard deviation less than 5 cm in the posterior distribution of the thickness parameter. In thick pack ice, we found an ice thickness of ~2.05 m and a standard deviation of ~30 cm in the PDF, but the values found from all inversions remain within a 6 cm interval, which suggests that the actual standard deviation is significantly less. All thickness estimations are consistent with measures made directly in the field (ice drillings, electromagnetic induction, ground penetrating radar).

Our investigations indicate that the proposed monitoring procedure exhibits similar performances when using 3 or 5 geophones, as long as the SNR allows a clear dispersion to be extracted from the waveforms of the icequakes. For example, thickness estimations remain within a 2 cm range in both cases. Of course, in configurations where 5 geophones are used instead of 3, the icequake location is better constrained, and consequently so is the ice thickness. However, the accuracy of the inferred parameters is comparable. Moreover, from the 60 array configurations tested in Section 3.1.2, it appears that different array geometries lead to similar results, so long as the stations in the array are not all near one another. In data where SNR is poorer and the extraction of the dispersion is more difficult, using 3 geophones may not always be sufficient for a successful inversion. Hence for optimal monitoring results, we prescribe the deployment of arrays of 4–5 geophones per 1 km<sup>2</sup> areas, where the stations configuration is such that it maximizes spatial coverage.

Despite the demonstrated accuracy and robustness of our approach, reducing the misfit between synthetic and field data is essential to reduce the uncertainty in the solution. For this reason, future works should focus on two main directions. The first one is the improvement of SNR, for example via the automatic selection and denoising of icequake waveforms for optimal results. To this end, machine learning-based approaches such as clustering or template matching, have proved very promising. The second one is the use of efficient forward models able to account for local variations of ice properties while keeping the computational cost to an acceptable level.

Our estimations of the ice thickness correspond to an average over the propagation paths between the icequake origin and the seismic stations. It is therefore expected to be applicable at all scales of icequake propagation, that is, any distance up to a few kilometers in the frequency range of the present study. However, an interesting perspective of this work is the study of remote rupture sources, potentially hundreds of kilometers away, by investigating wave propagation at much lower frequency with stations spaced by ~100 km. Most of what is known about sea ice deformation and fracturing comes from large scale (>10 km) satellite observations, such as the RADARSAT Geophysical Processor System dataset (Kwok, 1998) or from the analysis of Lagrangian trajectories (buoys; Rampal et al., 2008). Satellite imagery allows to highlight that large scale deformation is mostly accommodated at the scale of a few days by linear structures of large dimensions (up to the scale of the basin). These structures are likely to be brittle (Marsan et al., 2004). The temporal resolution of how the rupture occurs along such long structures is still lacking, but could be analyzed by exploiting similar methods as exposed here.

The use of icequakes presents the advantage of being a completely passive approach, without the need of active sources. Given the very large number recorded every hour (>500 both in pack ice and landfast ice), one can fairly expect them to originate from a large range of directions and distances around the stations. This would open the way toward exhaustive, time-dependent thickness tomographies of the ice, similar to the velocity tomographies of the crust. Moreover, the exploitation of the horizontal channels may pave the way toward simultaneous inversions of the ice thickness and elastic properties, potentially with only two stations. This can be achieved by including, in the cost function, the waveforms of the other two fundamental modes ( $SH_0$  and  $QS_0$ ).



A complementary perspective of this work is to apply the present method to the NCF instead of icequakes. As shown in Moreau et al. (2020), the correlation of seismic noise recorded at two stations for a few hours quickly converges toward the impulse response of sea ice between these stations. Since the relative position of the stations is known from GPS coordinates, the source-receiver station distance would be perfectly constrained, allowing for an even more accurate inversion of the ice thickness. The NCF also integrates the contribution of all seismic sources, impulsive or more stationary. It naturally results in more energetic waveforms than those from icequakes, which has potential to extend the scales at which ice thickness can be inferred.

### Data Availability Statement

The metadata of the dataset recorded in Svalbard are available at the following doi: <http://dx.doi.org/10.15778/RESIF.XG2019>. The full dataset (total size = 3.2 Tb) is available upon request to the corresponding author. A subset can be accessed instantly via a direct download link (25 Gb in size for each day). To request this link, please send an e-mail to [resif-dc@ujf-grenoble.fr](mailto:resif-dc@ujf-grenoble.fr) with your affiliation and IP address. This subset contains the continuous recordings of all stations on 1 and 5 March 2019, from which part of the results presented in this paper were obtained (with 3C stations data downsampled at 500 Hz). The dataset recorded on pack ice in the Arctic Ocean (a few Mb in size) is available upon request to the corresponding author.

### Acknowledgments

ISTerre is part of Labex OSUG@2020. This research was funded by the Agence Nationale de la Recherche (ANR, France), and by the Institut Polaire Français Paul-Emile Victor (IPEV). The authors would like to thank the associate editor and reviewers for the useful and constructive comments.

### References

- Anderson, D. L. (1958). Preliminary results and review of sea ice elasticity and related studies. *Transactions of the Engineering Institute of Canada*, 2, 116–122.
- Andrieu, C., & Moulines, E. (2006). On the ergodicity properties of some adaptive MCMC algorithms. *The Annals of Applied Probability*, 16(3), 1462–1505. <https://doi.org/10.1214/10505160600000286>
- Bochud, N., Vallet, Q., Minonzio, J. G., & Laugier, P. (2017). Predicting bone strength with ultrasonic guided waves. *Scientific Reports*, 7, 43628. <https://doi.org/10.1038/srep43628>
- Gascard, J.-C., le Goff, H., Weber, M., Bruemmer, B., Offermann, M., Doble, M., et al. (2008). Exploring Arctic transpolar drift during dramatic sea ice retreat. *EOS*, 89(3), 21–23. <https://doi.org/10.1029/2008EO030001>
- Hass, C., Le Goff, H., Audrain, S., Perovich, D., & Haapala, J. (2011). Comparison of seasonal sea-ice thickness change in the Transpolar Drift observed by local ice-mass balance observations and floe-scale EM surveys. *Annals of Glaciology*, 52, 97–102. <https://doi.org/10.3189/172756411795931778>
- Hunkins, K. (1960). Seismic studies of sea ice. *Journal of Geophysical Research*, 65(10), 3459–3472. <https://doi.org/10.1029/JZ065i010p03459>
- Kwok, R. (1998). The RADARSAT geophysical processor system. In C. Tsatsoulis & R. Kwok (Eds.), *Analysis of SAR data of the polar oceans* (pp. 235–257). Berlin, Heidelberg: Springer. [https://doi.org/10.1007/978-3-642-60282-5\\_11](https://doi.org/10.1007/978-3-642-60282-5_11)
- Marsan, D., Stern, H., Lindsay, R., & Weiss, J. (2004). Scale dependence and localization of the deformation of Arctic sea ice. *Physical Review Letters*, 93(17), 178501. <https://doi.org/10.1103/PhysRevLett.93.178501>
- Marsan, D., Weiss, J., Larose, E., & Métaixian, J.-P. (2012). Sea-ice thickness measurement based on the dispersion of ice swell. *Journal of the Acoustical Society of America*, 131(1), 80–91. <https://doi.org/10.1121/1.3662051>
- Marsan, D., Weiss, J., Métaixian, J.-P., Grangeon, J., Roux, P.-F., & Haapala, J. (2011). Low frequency bursts of horizontally-polarized waves in the Arctic sea-ice cover. *Journal of Glaciology*, 57(202), 231–237. <https://doi.org/10.3189/002214311796405834>
- Marsan, D., Weiss, J., Moreau, L., Gimbert, F., Doble, M., Larose, E., et al. (2019). Characterizing horizontally-polarized shear and infragravity vibrational modes in the Arctic sea ice cover using correlation methods. *Journal of the Acoustical Society of America*, 145(3), 1600–1608. <https://doi.org/10.1121/1.5094343>
- Mitra, M., & Gopalakrishnan, S. (2016). Guided wave based structural health monitoring: A review. *Smart Materials and Structures*, 14(5), 0964–1726. <https://doi.org/10.1088/0964-1726/25/5/053001>
- Moreau, L., Boué, P., Serripiéri, A., Weiss, J., Hollis, D., Pondaven, I., et al. (2020). Sea ice thickness and elastic properties from the analysis of multimodal guided wave propagation measured with a passive seismic array. *Journal of Geophysical Research: Oceans*, 125(4), e2019JC015709. <https://doi.org/10.1029/2019JC015709>
- Moreau, L., Lachaud, C., Théry, R., Predoi, M. V., Marsan, D., Weiss, J., et al. (2017a). Monitoring ice thickness and elastic properties from the measurement of leaky guided waves: A laboratory experiment. *Journal of the Acoustical Society of America*, 142(5), 2873–2880. <https://doi.org/10.1121/1.5009933>
- Moreau, L., Stehly, L., Boué, P., Lu, Y., Larose, E., & Campillo, M. (2017b). Improving ambient noise correlation functions with an SVD-based Wiener filter. *Geophysical Journal International*, 211(1), 418–426. <https://doi.org/10.1093/gji/ggx306>
- Rampal, P., Weiss, J., Marsan, D., Lindsay, R., & Stern, H. (2008). Scaling properties of sea ice deformation from buoy dispersion analyses. *Journal of Geophysical Research*, 113, C03002. <https://doi.org/10.1029/2007JC004143>
- Sabra, K. G., Gerstoft, P., Roux, P., Kuperman, W. A., & Fehler, M. C. (2005). Extracting time-domain Green's function estimates from ambient seismic noise. *Geophysical Research Letters*, 32, 79–84. <https://doi.org/10.1029/2004GL021862>
- Shapiro, N. M., & Campillo, M. (2004). Emergence of broadband Rayleigh waves from correlations of the ambient seismic noise. *Geophysical Research Letters*, 31, L07614. <https://doi.org/10.1029/2004GL019491>
- Stein, P. J., Euerle, S. E., & Parinella, J. C. (1998). Inversion of pack ice elastic wave data to obtain ice physical properties. *Journal of Geophysical Research*, 103(C10), 21783–21796.
- Tarantola, A. (2005). *Inverse problem theory and methods for model parameter estimation*. Philadelphia, PA: Society for Industrial and Applied Mathematics.

Vihma, T., Pirazzini, R., Fer, I., Renfrew, I. A., Sedlar, J., Tjernström, M., et al. (2014). Advances in understanding and parameterization of small-scale physical processes in the marine Arctic climate system: A review. *Atmospheric Chemistry and Physics*, *14*, 9403–9450. <https://doi.org/10.5194/acp-14-9403-2014>